



Adaptive control of laser-wakefield accelerators driven by mid-IR laser pulses

J. LIN,^{1*} Y. MA,¹ R. SCHWARTZ,² D. WOODBURY,² J. A. NEES,¹
M. MATHIS,¹ A. G. R. THOMAS,¹ K. KRUSHELNICK,¹ AND
H. MILCHBERG²

¹*Center for Ultrafast Optical Science, University of Michigan, Ann Arbor, MI 48109, USA*

²*Institute for Research in Electronics and Applied Physics, University of Maryland, College Park, MD 20742, USA*

*linjinp@umich.edu

Abstract: There has been growing interest both in studying high-intensity ultrafast laser plasma interactions with adaptive control systems as well as using long wavelength driver beams. We demonstrate the coherent control of the dynamics of laser-wakefield acceleration driven by ultrashort (~ 100 fs) mid-infrared ($\sim 3.9 \mu\text{m}$) laser pulses. The critical density at this wavelength is $7.3 \times 10^{19} \text{ cm}^{-3}$, which is achievable with an ordinary gas target system. Interactions between mid-infrared laser pulses and such near-critical-density plasma may be beneficial due to much higher absorption of laser energy. In addition, the normalized vector potential of the laser field a_0 increases with longer laser wavelength, lowering the required peak laser intensity to drive non-linear laser-wakefield acceleration. Here, MeV level, collimated electron beams with non-thermal, peaked energy spectra are generated. Optimization of electron beam qualities are realized through adaptive control of the laser wavefront. A genetic algorithm controlling a deformable mirror improves the electron total charge, energy spectra, beam pointing and stability at various plasma density profiles. Particle-in-cell simulations reveal that the optimal wavefront causes an earlier injection on the density up-ramp and thus higher energy gain as well as less filamentation during the interaction, which leads to the improvement in electron beam collimation and energy spectra.

© 2019 Optical Society of America under the terms of the [OSA Open Access Publishing Agreement](#)

1. Introduction

Coherent control of dynamic processes through systematic optimization of the phase of laser has been applied to a variety of systems, such as quantum dots [1, 2], qubits [3], two photon transitions [4], photocurrent generation [5] and chemical reactions [6]. In the field of intense laser-matter interactions, deformable mirrors (DMs) controlled by genetic algorithms (GAs) taking in feedback measurements have already been utilized widely in high power laser facilities. These adaptive optical systems have been implemented to control THz generation [7], multi-filament configuration [8], high order harmonic generation [9] and optimization of the focal spot [10–12]. Plasma waves produced from the interaction process can also be controlled via this phase shaping technique, suggesting that a particular laser wavefront can steer the plasma wave to a final state using an optimal electric field structure [13]. Plasma waves produced by high power lasers, in particular relativistic electrons from laser wakefield accelerators (LWFA), have been studied extensively [14–20] as it has extremely large accelerating gradients and consequently the short accelerating distance compared to conventional accelerators. There still remain issues with beam pointing, stability control, energy spread and dark current for use of such beams. In LWFA, plasma electrons are expelled from the relativistic laser pulse and form a cavity, or a void of electrons, behind the pulse. The cavity's spatial extent is close to a plasma wavelength in length, a laser focal spot size in width and close to the speed of light in phase velocity. Background electrons can get captured in the cavity and get accelerated to high energy. However, when the

laser power is high enough ($P > P_{cr}$), relativistic self-focusing modifies the laser wavefront to overcome diffraction limit and focuses the laser pulse to higher intensity or guides the beam, depending on the ratio P/P_{cr} . If the pulse length is long relative to the plasma wavelength, it also overlaps multiple plasma buckets and the laser pulse can modulate and break up into a train of short pulses with pulse length around the plasma wavelength. Operating in this self-modulated LWFA (SM-LWFA) regime with higher density, a large amplitude wakefield approaching the wave-breaking limit is generated to trap background electrons, but the acceleration length is limited. SM-LWFA has recently aroused interest in betatron radiation using picosecond duration laser pulses at large laser facilities [21]. Looking at the scaling in the mechanism, the critical power [22], as well as the ponderomotive force (electromagnetic energy density gradient) that pushes the electrons outwards and drives the wakefields [23], are both dependent on the square of laser wavelength:

$$P_{cr} = 17.4n_{cr}/n_e[\text{GW}] \quad F_p = -m_e\gamma c^2\nabla(a^2/2) \quad (1)$$

where n_e is the electron density, m_e is the electron mass, $n_{cr} = \frac{4\pi^2 m_e \epsilon_0 c^2}{e^2} \frac{1}{\lambda^2} \propto \lambda^{-2}$ is the critical plasma density and a^2 is the normalized laser intensity with a peak amplitude of the normalized vector potential $a_0 = 8.6 \times 10^{-10} \lambda [\mu\text{m}] \sqrt{I [\text{W/cm}^2]} \propto \lambda$. For example, looking at laser wavelength $\lambda = 0.8 \mu\text{m}$ and $3.9 \mu\text{m}$, the critical densities are $2 \times 10^{21} \text{ cm}^{-3}$ and $7 \times 10^{19} \text{ cm}^{-3}$, respectively. Assuming an electron density of $3 \times 10^{19} \text{ cm}^{-3}$, the critical powers are 987 GW and 42 GW, respectively. Over the past decade, remarkable progress has been made in the generation [24, 25] and application of mid-infrared (MIR) laser pulses, showing their superiority in generating high order harmonics [26, 27], electromagnetic pulses [28], filaments [29] and x-rays [30]. For instance, it has been found that the characteristic k_α flux of hard x-rays from $3.9 \mu\text{m}$ laser driver is much greater than that from the 800 nm driver [30]. Reaching longer wavelengths in LWFA has also drawn attention, not only for its lower critical power threshold and higher a_0 but also for being less difficult in achieving near critical density interactions, which enables the generation of MeV-scale electrons with moderate laser intensity. These MeV-scale electron sources from high repetition rate laser systems have demonstrated their use in electron radiography [31, 32]. SM-LWFA at near critical density has been approached with a mid-infrared laser at $\lambda = 3.9 \mu\text{m}$ and moderate density gas jets [33], compared to the experiments using 800nm Ti:Sapphire laser with cryogenically cooled, high density gas jets [34, 35].

It is natural to consider coherent control of the LWFA dynamics with mid-IR lasers. In this work, we present the first experiment to optimize the quality of the electron beam from mid-IR ($\lambda = 3.9 \mu\text{m}$) light interacting with near-critical density plasma. Beam charge, energy spectrum, beam pointing and fluctuation have been improved by controlling the laser wavefront via an evolutionary algorithm. Wavefront reconstruction and PIC simulations illustrate that changes on laser wavefront lead to different laser focusing and self-guiding in plasma. Filamentation has been observed in the case of a flat laser wavefront, and can be corrected by the adaptive control system for better electron acceleration. This work also demonstrates the ability to have regular deformable mirrors with $4 \mu\text{m}$ full stroke to properly function in a mid-IR laser system, and the ability to reconstruct wavefronts without the presence of a mid-IR wavefront sensor.

2. Results

2.1. Experimental setup

The experiment was conducted at the University of Maryland, using a hybrid optical parametric amplifier/optical parametric chirped pulse amplifier (OPA/OPCPA) laser system which generates $25 \pm 1 \text{ mJ}$, 87 fs, $3.9 \mu\text{m}$ pulses at a repetition of 20 Hz [24]. A deformable mirror (DM) controlled by the evolutionary algorithm was used to adjust the laser wavefront based on the diagnostic feedback. The experiment setup is shown in Fig. 1. An f/2.7 focus was achieved

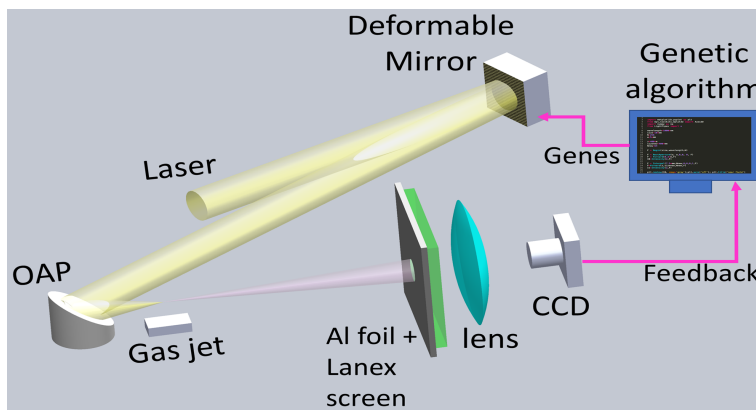


Fig. 1. Schematic of the setup: Deformable mirror: AOA Xenitics 37-channel 2 inch; OAP: f/2.7; Gas jet: $150\mu\text{m}$ orifice diameter nozzle; CCD: The Imaging Source DMK41BU02.H Charged Particle Device (CCD) camera; Lanex: LANEX Regular screen.

from the paraboloid and the 37.5mm diameter laser beam was focused to $15\mu\text{m}$ at the beam waist, measured using a knife-edge scan. The pulse energy on target was measured to be 15 mJ, resulting a peak intensity $I = \frac{0.88 \cdot E_p}{\tau_p \cdot \pi \cdot w^2 / 2} = 4.3 \times 10^{16} \text{ W/cm}^2$ and $a_0 \sim 0.7$. Plasma density up to $3 \times 10^{19} \text{ cm}^{-3}$ (or 40% of the critical density at $\lambda = 3.9\mu\text{m}$) can be easily reached by the gas jet without cryogenic cooling. The jet was mounted onto a 3-D translation stage to adjust the position of the laser focus throughout the hydrogen gas target. A LANEX regular screen with a shield of $100\mu\text{m}$ thick aluminum was placed 9 cm from the jet and imaged onto the CCD camera. The camera was synchronized to the $3.9\mu\text{m}$ pulse and integrated over 2 ms. In each iteration, the genetic algorithm analyzed 50 electron beam profiles corresponding to 50 deformable mirror surfaces, and the median of 10 shots was used to evaluate a figure of merit function for each mirror surface. While the system repetition rate was limited to 1 Hz due to radiation safety requirements, this was still adequate for averaging over the shot-to-shot fluctuation while keeping the data acquisition period reasonable. The starting point of the optimization process was chosen at the condition of minimum phase changes, where the DM was initialized to a flat mirror surface. It took the evolutionary algorithm ~ 30 iterations to find an improved mirror surface where the generation curve approached convergence, as is shown in Fig. 2.

2.2. Optimizing the electron total charge

Figure 2(a) illustrates the improving curves using total charge as FOM with laser focus at different positions on the Gaussian gas density profile (FWHM $\sim 250 - 1000\mu\text{m}$ [33]). Note that the low energy electrons (< 500 keV) were filtered by the aluminum foil and the total charge collected was ~ 450 pC. The gas jet was moved in $10-\mu\text{m}$ -step along the laser direction. A Nomarski interferometer with 515 nm probe light indicated that the plasma density was 37%, 35% and 29% of critical density at the front, center and back side of the gas jet.

Electron energy spectra were compared at different focusing positions before and after optimization in Fig. 3(a)-3(e), while examples of raw energy spectra are shown in Fig. 3(f). A high energy bump around 3 MeV shows up in some individual shots for the back focus, and gets lower and weaker as the focus moves towards the front of the density ramp. Improvements are observed at all three focal positions and focusing at the center ($0.35n_{cr}$) gives the best energy spectrum. Focusing on the back ($0.29n_{cr}$) gives very high beam charges, shown in Fig. 2(a),

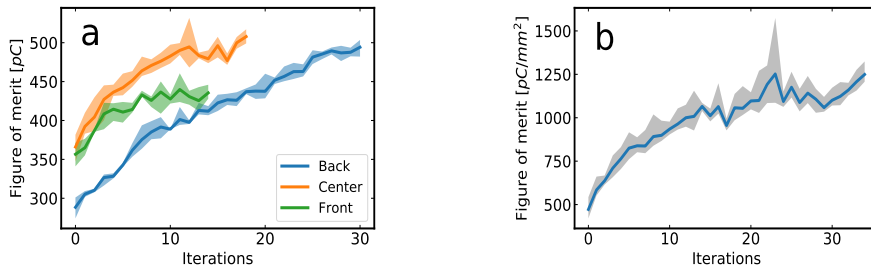


Fig. 2. Improvement charts using different figure of merit (FOM) functions: (a) total charge collected in the region of interest on CCD image after background subtraction; (b) the fitness function defined in Eq. (2) with $n=2$. Both optimizations started from initializing the deformable mirror to a flat surface. The shaded area refers to the variation of 5 best genes in each iteration. The number of iteration was limited by the experimental time considering the system repetition rate was as low as 1 Hz. The figure of merit values were calibrated to real units taking into account the geometry and the efficiency of optics, LANEX [36] and CCD.

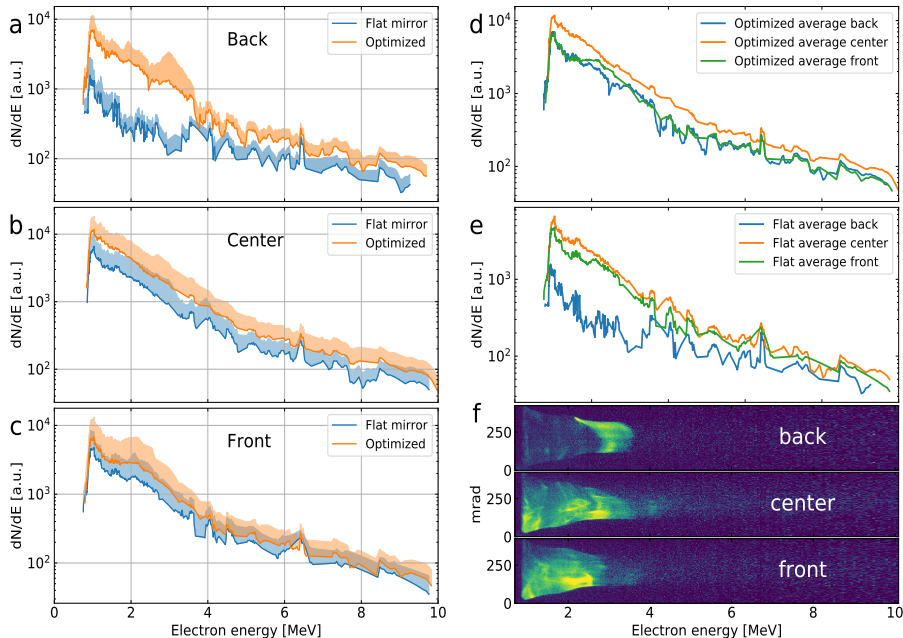


Fig. 3. Comparison of electron beam energy spectra: (a)-(c) before and after optimization; (d),(e) at front, center and back of the gas jet. 20 consecutive images were taken in each case. The shot-to-shot variation is shown in (a)-(c) while the statistic mean was shown in (d),(e). Examples of raw spectra with non-thermal peak features are shown in (f), in which the optimal laser wavefront found by the genetic algorithm was focused at back, center and front of the gas jet. Note that peaks do not occur on all shots.

but worse energy spectrum. This could be caused by the electron beam missing the slit of the spectrometer, due to inferior beam collimation and pointing stability. The trend in Fig. 3 indicates

the existence of an optimal plasma density for electron acceleration in the mid-IR regime, as was mentioned by Woodbury [33].

2.3. Optimizing the electron beam profile

To further improve the quality of the electron beam profile, the image moment function, as is defined in Eq. (2), was applied to the genetic algorithm.

$$FOM = \sum_{(i,j)}^{r_{ij} \neq r_0} \frac{I_{ij}}{|r_{ij} - r_0|^n} \quad (2)$$

where I_{ij} is the intensity collected at pixel position r_{ij} on the camera. The beam center r_0 is determined in each shot from the center of mass calculation after background subtraction. It quantifies not only the total charge but also beam collimation and pointing. The improvement chart is shown in Fig. 2(b) and the optimization performance is shown in Fig. 4. The genetic algorithm started from initializing the DM to a flat surface. It is observed that the raw images in Fig. 4(a) are divergent and have significant pointing fluctuations while the ones in Fig. 4(b) are collimated and directional. Detailed analysis can be found in Fig. 4(c)-4(f). Averaging over 30 shots, the optimization was able to increase the total beam charge by $\sim 40\%$ and the peak charge density to threefold in 35 iterations. In Fig. 4(e) the beam divergence θ_x and θ_y in transverse directions were reduced from 206 ± 64 mrad and 228 ± 69 mrad to 128 ± 21 mrad and 110 ± 20 mrad, respectively. The pointing instabilities, defined as the standard deviations of beam pointing $\delta\theta_x$ and $\delta\theta_y$ in Fig. 4(f), were reduced from 25.2 mrad and 45.7 mrad to 14.5 mrad and 20.6 mrad.

2.4. Wavefront reconstruction

The laser wavefront was measured *ex situ* by applying the recorded voltage distribution on the deformable mirror and subsequently measuring the wavefront with visible light. An imaging system involving the deformable mirror and a Shack-Hartman wavefront sensor was set up using a helium-neon laser after the experiment. The FrontSurfer wavefront analyzer (Version 1.4.7, OKO Technologies), consisting of a high-precision lenslet array and a CMOS UI-2210M CCD camera, can describe the wavefront in Zernike polynomials up to 200th order:

$$\Delta\phi = \sum_{j=1}^{200} A_j Z_j \quad (3)$$

where A_j and Z_j represent the j^{th} coefficient and base of the Zernike polynomials, respectively. Knowing the voltages on the deformable mirror, the coefficients could be obtained from the influence matrix C_{ij} :

$$A_j = \sum_{i=1}^{37} C_{ij} V_i \quad (4)$$

The influence matrix method is useful for real-time analysis of the wavefront, but here only the optimized wavefront is to be analyzed. Instead of measuring each element in the influence matrix, an alternative way to restore the wavefront change due to the DM (ϕ_{DM}) is to directly apply the voltage recorded in experiment and measure the mirror surface. A reference mirror surface with a known wavefront would be necessary to reconstruct the $3.9\mu\text{m}$ laser wavefront. Analogous to the setup in Fig. 1, the laser beam was attenuated and focused onto an AGS crystal to generate second harmonic (SH) signal. The genetic algorithm was run to improve the SH signal to threefold till convergence, which suggested the highest peak intensity available [10]. It corresponds to the smallest focal spot and the flattest wavefront available. A knife edge scan showed the focal spot

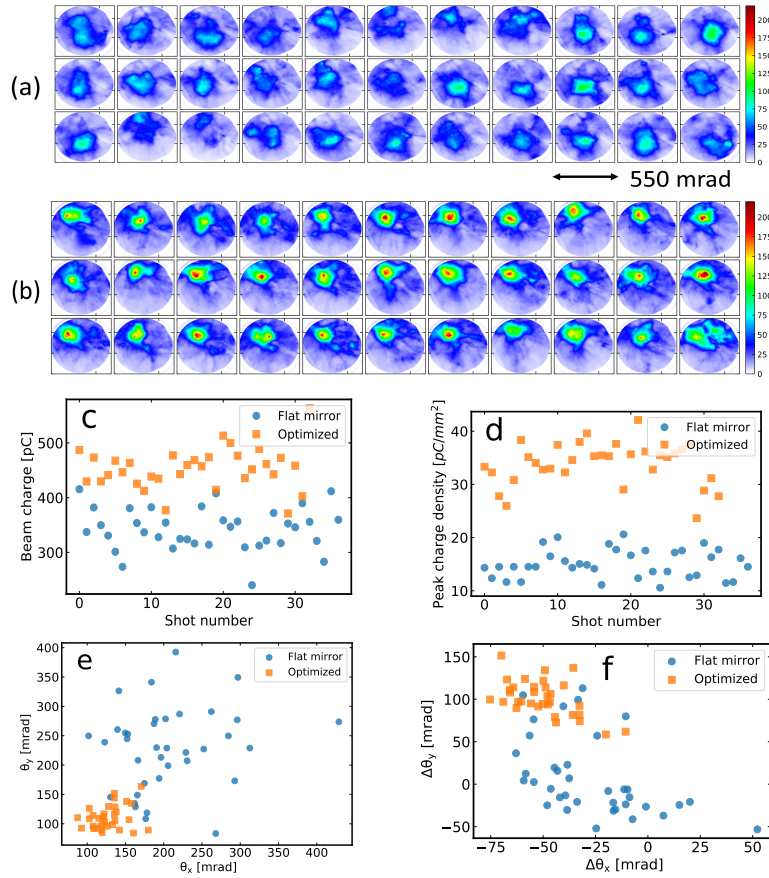


Fig. 4. Electron beam profile optimization using the image moment as figure of merit, defined in Eq. (2). (a) and (b): 30 consecutive raw images before and after optimization. The circular edge, due to a collimation tube in front of the LANEX, corresponds to a solid angle of 550 mrad. (c) - (f) are the visualization of beam quality in terms of total beam charge, peak charge density, divergence angle and beam pointing, respectively. Each dot represents one shot.

was decreased from $\sim 25\mu\text{m}$ to $\sim 15\mu\text{m}$ after the second harmonic optimization. This voltage map on the DM was recorded and afterwards applied to the wavefront analysis system with visible light to obtain the phase ϕ_{SHG} . Assuming the laser wavefront going into the DM was ϕ_{laser} , the phase at the SHG optimized deformable mirror shape would be:

$$\phi = \phi_{laser} + 2 \times \phi_{SHG} \approx \phi_{Gaussian} \quad (5)$$

On the other hand when the DM was set to optimize the electron beam, the :

$$\phi_{opt} = \phi_{laser} + 2 \times \phi_{DM} \quad (6)$$

Subtracting Eq. (5) from Eq. (6) would give the laser wavefront leaving the deformable mirror during the experiment, $2 \times (\phi_{DM} - \phi_{SHG})$, as is shown in Fig. 5(a). Fresnel diffraction was taken into account to propagate the wavefront 4.5 meters to the OAP, as is shown in Fig. 5(b), and the phase change was calculated with LightPipes [37] using direct integration approach.

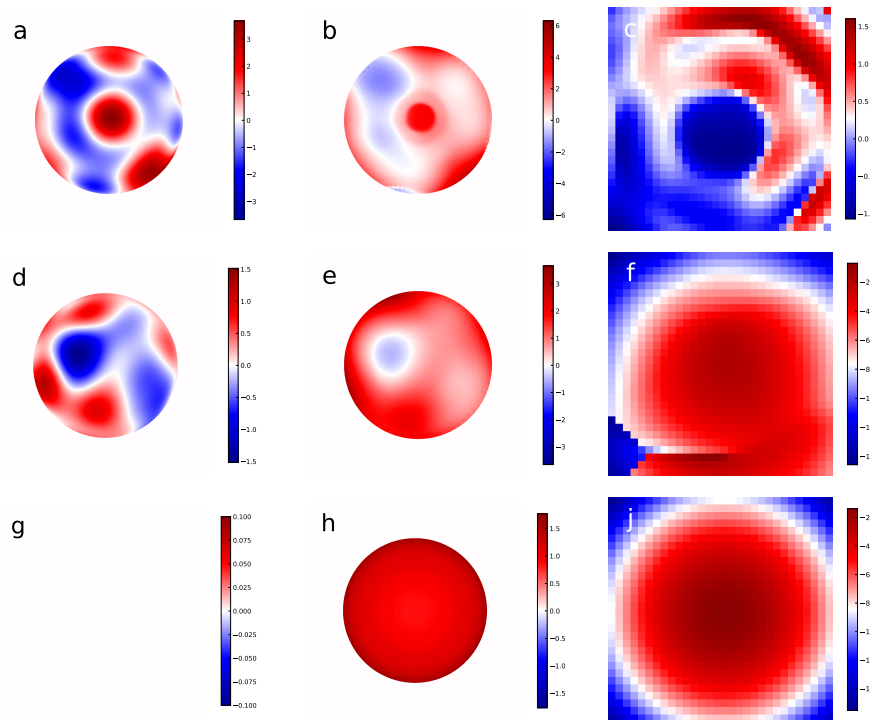


Fig. 5. Reconstruct the laser wavefront propagation for three cases. (a-c): wavefront for the optimal electron beam, (d-f): wavefront from a flat mirror surface, and (g-i): perfect Gaussian wavefront. Wavefronts leaving the DM, propagating 4.5m and focused by the OAP are shown in the first, second and third column. First 50 Zernike coefficients are included in the reconstruction.

Figure 5(c) shows the wavefront at $500 \mu\text{m}$ before the geometric focus, which was used in the PIC simulation. Figure 5(d)-5(f) present the laser wavefront before the evolutionary algorithm was run where the DM was initialized to a flat surface. The propagation of a perfect Gaussian beam is included in Fig. 5(g)-5(i) for comparison. Note that the validity of this whole reconstruction process is dependent on a list of factors, including the stability of the voltage on the DM actuators, the accuracy of measurement using the visible wavefront sensor, and mostly the flatness of the wavefront after the second harmonic optimization, or the validity of Eq. (5).

2.5. Numerical simulations

The effect of wavefront changes on wakefield acceleration was further investigated with two-dimensional (2D) particle-in-cell (PIC) simulations in the EPOCH framework [38]. The simulation box with moving window is $200 \mu\text{m} \times 160 \mu\text{m}$ with grid size of 1/32 and 1/16 λ_L in x and y , where $\lambda_L = 3.9 \mu\text{m}$ is the laser wavelength, x is the laser propagation direction, y is the transverse direction and z is the laser polarization direction. There are 64 macro-particles per cell. The laser pulse is Gaussian in both transverse and longitudinal directions with a FWHM pulse duration $\tau = 100 \text{ fs}$, a $1/e^2$ spot size $w_0 = 13 \mu\text{m}$ and a normalized vector potential $a_0 = 0.7$. The plasma density distribution along the laser propagation direction was fitted from interferometric measurements which indicate a Gaussian distribution with a peak density of $0.4 n_c$ and a FWHM of $505 \mu\text{m}$, as shown in Fig. 6(a). The focus position of the laser pulse was initially set at $374 \mu\text{m}$, which corresponds to the “Center” case, for a perfect Gaussian laser beam. In PIC simulations,

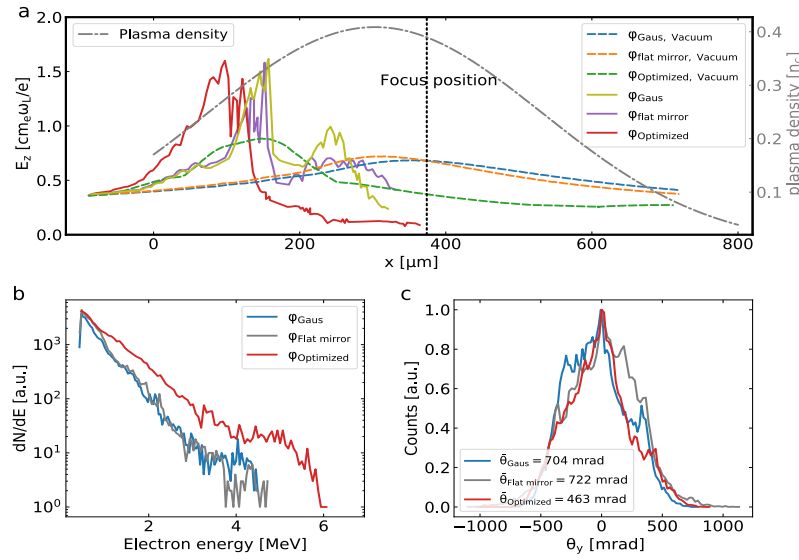


Fig. 6. Laser field evolution and electron beam qualities with different laser wavefronts in PIC simulations. (a) Evolution of peak laser field strength with different wavefronts in vacuum and plasma, respectively. (b) and (c) Electron spectra and angular distributions at the end of the simulation ($t = 2$ ps) with different laser wavefronts and the same plasma profile showing in (a).

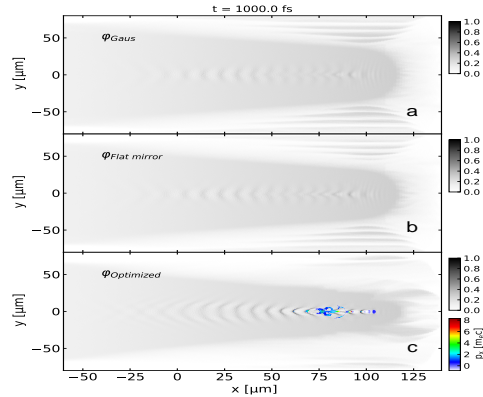


Fig. 7. Snapshot for plasma density and electron beam distribution with (a) Gaussian, (b) flat mirror and (c) optimized wavefront at the same time, $t = 1$ ps. Self-injection has occurred with optimized wavefront in (c) while not in the other two cases.

we compared three different cases, namely “Optimized”, “Flat mirror” and “Gaussian”, with wavefronts shown in Fig. 5(c), 5(f) and 5(j), respectively.

The propagation of laser pulses with different wavefronts in both vacuum and plasma were examined. As shown in Fig. 6(a), the peak laser field strength reaches its maximum much earlier in the optimized wavefront case than in the other cases. The LWFA process starts as the laser field reaches its maximum during the self-focusing, and almost the whole acceleration happens within

the density up-ramp region. The laser pulse with optimized wavefront initiates the acceleration earlier, as is shown in Fig. 7, and thus experiences a lower plasma density. Since the maximum energy gain of LWFA [39] scales as $\Delta E_{max} \propto n_p^{-2/3}$, the relative lower plasma density for the “Optimized” case would result in higher final energy gain. This has been confirmed by the electron spectra at the end of the simulations, as shown in Fig. 6(b). The electron spectra from PIC simulations agree with the experimental results in Fig. 3 qualitatively.

Moreover, the laser pulses in the “Gaussian” and “Flat mirror” cases suffer more from the transverse self-modulation, leading to the self-filamentation shown in Fig. 8(a) and (c). These filaments are intense enough to drive LWFA on their own, which eventually lead to the wing structure of the electron beam in Fig. 8(b) and (d). As a consequence, the electron beam collimation in these two cases is worse than that in the “Optimized” case, as is presented in Fig. 6(c), which also agrees with the experimental results.

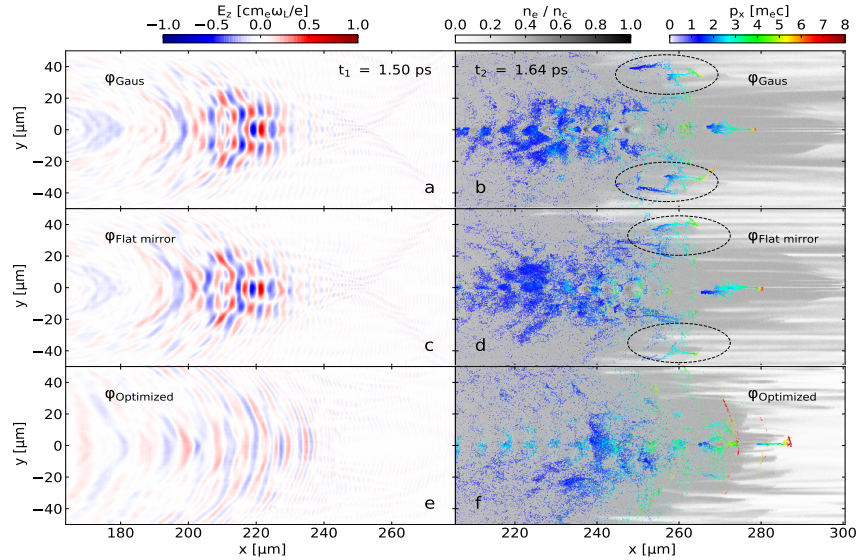


Fig. 8. Snapshots of PIC simulations with different wavefronts. Laser field distribution at $t = 1.5$ ps for (a) Gaussian, (c) Flat mirror and (e) Optimized wavefront, respectively. Plasma density distribution at $t = 1.64$ ps for (b) Gaussian, (d) Flat mirror and (f) Optimized wavefront, respectively. Spatial distribution of accelerated electron macro-particles are overlaid on the plasma density distribution where color scale represents longitudinal momentum of the particles.

3. Discussion

Understanding the phase front condition of the laser to the plasma is crucial to the success of wakefield acceleration. The non-Gaussian features of laser wavefront in experiments can strongly affect the acceleration mechanism and betatron sources [40]. It is, therefore, of great interest to control the phase front in LWFA. Optical steering of the electron beam direction [41], enhancement of betatron radiation [42] and spectral control of the x-rays produced in the process [43] have been achieved by modifying the laser wavefront. Here we have demonstrated the ability to coherently control the relativistic electron beam from wakefield acceleration by mid-IR laser pulses in near-critical density plasma. Electron total charge, energy spectrum, beam pointing and fluctuation are improved and the effect of wavefront changes on acceleration process

are studied with PIC simulation. The optimal wavefront initiates the acceleration earlier on the density up-ramp and thus experiences a lower plasma density, which leads to higher energy gain during the interaction. It also sees less filamentation from the transverse self-modulation, which would be responsible for the wing structure and divergence of the electron beam. With this improved wavefront, better electron beam collimation and energy spectra are observed in both experiment and simulation. The computer modelling is based on wavefront reconstruction using the voltage applied to the deformable mirror, in absence of a mid-IR wavefront sensor.

Improvement in electron beam quality is independent from the improvement in laser focus since the highest intensity laser focus produced an order of magnitude lower electron charge. This behavior, together with the intensity wings from optimized wavefront, has been observed in previous work [13] with $\lambda = 800\text{nm}$ as well. Analogously, looking at the x-rays producing by the wakefield acceleration, a wavefront with coma aberration generates more high-energy photons than a flat wavefront [43] does. Modifying the phase of the light can cause strong optical nonlinear effects in the plasma interactions, which can affect the plasma wave dynamics in a complex but deterministic manner.

This work opens a new window to the study of coherent control of mid-IR laser plasma interaction. It is worth noting that the full stroke of the deformable mirror surface is $4\ \mu\text{m}$, or a wavelength of the mid-IR driver. Namely, without upgrading the DMs to deeper stroke or the wavefront sensors to a longer wavelength range, current adaptive optical systems are capable of conducting experiments using mid-IR lasers. Our work shows the potential for the use of long wavelength lasers in LWFA in near-critical density plasma which would be difficult to achieve using near-IR lasers. Recently, pulse shaping implemented into the system algorithm [44] has been validated using near-IR lasers and can be extended to the mid-IR critical-density regime. Future work could also include a theoretical validation of the wavefront reconstruction approach by means of the quantum optimal control theory (QOCT) [45].

Funding

Air Force Office of Scientific Research (AFSOR) (FA9550-16-1-0121, FA9550-16-1-0259, NSF grant 1535628, NSF PHY-1619582, DOE grant DE-SC0016804, DE-SC0015516); UK EPSRC (EP/G054950/1, EP/G056803/1, EP/G055165/1, EP/M022463/1); DOE NNSA SSGF program (DE-NA0003864).

Acknowledgments

J. Lin thanks Peter Kordell for insightful conversation in the wavefront reconstruction process.

References

1. N. H. Bonadeo, J. Erland, D. Gammon, D. Park, D. Katzer, and D. Steel, "Coherent optical control of the quantum state of a single quantum dot," *Science* **282**, 1473–1476 (1998).
2. K. C. Nowack, F. Koppens, Y. V. Nazarov, and L. Vandersypen, "Coherent control of a single electron spin with electric fields," *Science* **318**, 1430–1433 (2007).
3. Y. Nakamura, Y. A. Pashkin, and J. Tsai, "Coherent control of macroscopic quantum states in a single-cooper-pair box," *Nature* **398**, 786 (1999).
4. D. Meshulach and Y. Silberberg, "Coherent quantum control of two-photon transitions by a femtosecond laser pulse," *Nature* **396**, 239 (1998).
5. A. Haché, Y. Kostoulas, R. Atanasov, J. Hughes, J. Sipe, and H. Van Driel, "Observation of coherently controlled photocurrent in unbiased, bulk gaas," *Phys. Rev. Lett.* **78**, 306 (1997).
6. A. Assion, T. Baumert, M. Bergt, T. Brixner, B. Kiefer, V. Seyfried, M. Strehle, and G. Gerber, "Control of chemical reactions by feedback-optimized phase-shaped femtosecond laser pulses," *Science* **282**, 919–922 (1998).
7. J. Hah, W. Jiang, Z. He, J. Nees, B. Hou, A. Thomas, and K. Krushelnick, "Enhancement of the generation by feedback-optimized wavefront manipulation," *Opt. Express* **25**, 17271–17279 (2017).
8. A. C. Englesbe, Z. He, J. A. Nees, A. G. Thomas, A. Schmitt-Sody, and K. Krushelnick, "Control of the configuration of multiple femtosecond filaments in air by adaptive wavefront manipulation," *Opt. Express* **24**, 6071–6082 (2016).

9. Y. Wang, T. Guo, J. Li, J. Zhao, Y. Yin, X. Ren, J. Li, Y. Wu, M. Weidman, Z. Chang, M. F. Jager, C. J. Kaplan, R. Geneaux, C. Ott, D. M. Neumark, and S. R. Leone, "Enhanced high-order harmonic generation driven by a wavefront corrected high-energy laser," *J. Phys. B: At. Mol. Opt. Phys.* **51**, 134005 (2018).
10. O. Albert, H. Wang, D. Liu, Z. Chang, and G. Mourou, "Generation of relativistic intensity pulses at a kilohertz repetition rate," *Opt. Lett.* **25**, 1125–1127 (2000).
11. S.-W. Bahk, P. Rousseau, T. Planchon, V. Chvykov, G. Kalintchenko, A. Maksimchuk, G. Mourou, and V. Yanovsky, "Generation and characterization of the highest laser intensities (10²² w/cm²)," *Opt. Lett.* **29**, 2837–2839 (2004).
12. J. Lin, J. H. Easter, K. Krushelnick, M. Mathis, J. Dong, A. Thomas, and J. Nees, "Focus optimization at relativistic intensity with high numerical aperture and adaptive optics," *Opt. Commun.* **421**, 79–82 (2018).
13. Z.-H. He, B. Hou, V. Lebailly, J. Nees, K. Krushelnick, and A. Thomas, "Coherent control of plasma dynamics," *Nat. Commun.* **6**, 7156 (2015).
14. T. Tajima and J. M. Dawson, "Laser electron accelerator," *Phys. Rev. Lett.* **43**, 267 (1979).
15. S. P. Mangles, C. D. Murphy, Z. Najmudin, A. G. Thomas, J. L. Collier, A. E. Dangor, E. J. Divall, P. S. Foster, J. G. Gallacher, C. J. Hooker, D. A. Jaroszynski, A. J. Langley, W. B. Mori, P. A. Norreys, F. S. Tsung, R. Viskup, B. R. Walton, and K. Krushelnick, "Monoenergetic beams of relativistic electrons from intense laser-plasma interactions," *Nature* **431**, 535 (2004).
16. C. Geddes, C. Toth, J. Van Tilborg, E. Esarey, C. Schroeder, D. Bruhwiler, C. Nieter, J. Cary, and W. Leemans, "High-quality electron beams from a laser wakefield accelerator using plasma-channel guiding," *Nature* **431**, 538 (2004).
17. J. Faure, Y. Glinec, A. Pukhov, S. Kiselev, S. Gordienko, E. Lefebvre, J.-P. Rousseau, F. Burgay, and V. Malka, "A laser-plasma accelerator producing monoenergetic electron beams," *Nature* **431**, 541 (2004).
18. E. Esarey, C. Schroeder, and W. Leemans, "Physics of laser-driven plasma-based electron accelerators," *Rev. Mod. Phys.* **81**, 1229 (2009).
19. W. P. Leemans, B. Nagler, A. J. Gonsalves, C. Toth, K. Nakamura, C. G. Geddes, E. Esarey, C. Schroeder, and S. Hooker, "Gev electron beams from a centimetre-scale accelerator," *Nat. Phys.* **2**, 696 (2006).
20. J. S. Liu, C. Q. Xia, W. T. Wang, H. Y. Lu, C. Wang, A. H. Deng, W. T. Li, H. Zhang, X. Y. Liang, Y. X. Leng, X. M. Lu, C. Wang, J. Z. Wang, K. Nakajima, R. X. Li, and Z. Z. Xu, "All-optical cascaded laser wakefield accelerator using ionization-induced injection," *Phys. Rev. Lett.* **107**, 035001 (2011).
21. F. Albert, N. Lemos, J. L. Shaw, P. M. King, B. B. Pollock, C. Goyon, W. Schumaker, A. M. Saunders, K. A. Marsh, A. Pak, J. E. Ralph, J. L. Martins, L. D. Amorim, R. W. Falcone, S. H. Glenzer, J. D. Moody, and C. Joshi, "Betatron x-ray radiation in the self-modulated laser wakefield acceleration regime: Prospects for a novel probe at large scale laser facilities," *Nucl. Fusion* **59**, 032003 (2019).
22. P. Sprangle, C.-M. Tang, and E. Esarey, "Relativistic self focusing of short pulse radiation beams in plasmas." Tech. rep., BERKELEY SCHOLARS INC SPRINGFIELD VA (1987).
23. W. Krueer, *The physics of laser plasma interactions* (Chemical Rubber Company, 2018).
24. G. Andriukaitis, T. Balčiūnas, S. Ališauskas, A. Pugžlys, A. Baltuška, T. Popmintchev, M.-C. Chen, M. M. Murnane, and H. C. Kapteyn, "90 gw peak power few-cycle mid-infrared pulses from an optical parametric amplifier," *Opt. Lett.* **36**, 2755–2757 (2011).
25. H. Liang, P. Krogen, Z. Wang, H. Park, T. Kroh, K. Zawilski, P. Schunemann, J. Moses, L. F. Dimauro, F. X. Kärtner, and K. H. Hong, "High-energy mid-infrared sub-cycle pulse synthesis from a parametric amplifier," *Nat. Commun.* **8**, 141 (2017).
26. T. Popmintchev, M. C. Chen, D. Popmintchev, P. Arpin, S. Brown, S. Ališauskas, G. Andriukaitis, T. Balčiūnas, O. D. Mücke, A. Pugžlys, A. Baltuška, B. Shim, S. E. Schrauth, A. Gaeta, C. Hernández-García, L. Plaja, A. Becker, A. Jaron-Becker, M. M. Murnane, and H. C. Kapteyn, "Bright coherent ultrahigh harmonics in the kev x-ray regime from mid-infrared femtosecond lasers," *Science* **336**, 1287–1291 (2012).
27. A. Mitrofanov, D. Sidorov-Biryukov, M. Rozhko, S. Ryabchuk, A. Voronin, and A. Zheltikov, "High-order harmonic generation from a solid-surface plasma by relativistic-intensity sub-100-fs mid-infrared pulses," *Opt. Lett.* **43**, 5571–5574 (2018).
28. A. Zheltikov and R. Nevels, "Intensity and wavelength scaling of laser-driven electron transition radiation: toward a table-top source of electromagnetic pulses," *Laser Phys. Lett.* **16**, 015401 (2018).
29. M. Burger, P. J. Skrodzki, J. Lin, J. Nees, K. Krushelnick, and I. Jovanovic, "Intense laser filament-solid interactions from near-ultraviolet to mid-infrared," *Opt. Express* **26**, 16456–16465 (2018).
30. J. Weisshaupt, V. Juvé, M. Holtz, S. Ku, M. Woerner, T. Elsaesser, S. Ališauskas, A. Pugžlys, and A. Baltuška, "High-brightness table-top hard x-ray source driven by sub-100-femtosecond mid-infrared pulses," *Nat. Photonics* **8**, 927 (2014).
31. S. P. Mangles, B. R. Walton, Z. Najmudin, A. E. Dangor, K. Krushelnick, V. Malka, M. Mancossi, N. Lopes, C. Carias, G. Mendes, and F. Dorchies, "Table-top laser-plasma acceleration as an electron radiography source," *Laser Part. Beams* **24**, 185–190 (2006).
32. G. Bussolino, A. Faenov, A. Giulietti, D. Giulietti, P. Koester, L. Labate, T. Levato, T. Pikuz, and L. Gizzi, "Electron radiography using a table-top laser-cluster plasma accelerator," *J. Phys. D: Appl. Phys.* **46**, 245501 (2013).
33. D. Woodbury, L. Feder, V. Shumakova, C. Gollner, R. Schwartz, B. Miao, F. Salehi, A. Korolov, A. Pugžlys, A. Baltuška, and H. M. Milchberg, "Laser wakefield acceleration with mid-ir laser pulses," *Opt. Lett.* **43**, 1131–1134 (2018).

34. A. Goers, G. Hine, L. Feder, B. Miao, F. Salehi, J. Wahlstrand, and H. Milchberg, "Multi-mev electron acceleration by subterawatt laser pulses," *Phys. Rev. Lett.* **115**, 194802 (2015).
35. F. Salehi, A. Goers, G. Hine, L. Feder, D. Kuk, B. Miao, D. Woodbury, K.-Y. Kim, and H. Milchberg, "Mev electron acceleration at 1 khz with < 10 mj laser pulses," *Opt. Lett.* **42**, 215–218 (2017).
36. Y. Glinec, J. Faure, A. Guemnie-Tafo, V. Malka, H. Monard, J. Larbre, V. De Waele, J. Marignier, and M. Mostafavi, "Absolute calibration for a broad range single shot electron spectrometer," *Rev. Sci. Instruments* **77**, 103301 (2006).
37. Gleb Vdovin, Fred van Goor, and Guyskk, "LightPipes: beam propagation toolbox," <https://opticspy.github.io/lightpipes>.
38. T. D. Arber, K. Bennett, C. S. Brady, A. Lawrence-Douglas, M. G. Ramsay, N. J. Sircombe, P. Gillies, R. G. Evans, H. Schmitz, A. R. Bell, and C. P. Ridgers, "Contemporary particle-in-cell approach to laser-plasma modelling," *Plasma Phys. Control. Fusion* **57**, 113001 (2015).
39. W. Lu, M. Tzoufras, C. Joshi, F. Tsung, W. Mori, J. Vieira, R. Fonseca, and L. Silva, "Generating multi-gev electron bunches using single stage laser wakefield acceleration in a 3d nonlinear regime," *Phys. Rev. Special Top. Beams* **10**, 061301 (2007).
40. J. Ferri, X. Davoine, S. Fourmaux, J. Kieffer, S. Corde, K. T. Phuoc, and A. Lifschitz, "Effect of experimental laser imperfections on laser wakefield acceleration and betatron source," *Sci. Reports* **6**, 27846 (2016).
41. A. Popp, J. Vieira, J. Osterhoff, Z. Major, R. Hörllein, M. Fuchs, R. Weingartner, T. P. Rowlands-Rees, M. Marti, R. A. Fonseca, S. F. Martins, L. O. Silva, S. M. Hooker, F. Krausz, F. Grüner, and S. Karsch, "All-optical steering of laser-wakefield-accelerated electron beams," *Phys. Rev. Lett.* **105**, 215001 (2010).
42. C. Yu, J. Liu, W. Wang, W. Li, R. Qi, Z. Zhang, Z. Qin, J. Liu, M. Fang, K. Feng, Y. Wu, L. Ke, Y. Chen, C. Wang, Y. Xu, Y. Leng, C. Xia, R. Li, and Z. Xu, "Enhanced betatron radiation by steering a laser-driven plasma wakefield with a tilted shock front," *Appl. Phys. Lett.* **112**, 133503 (2018).
43. S. P. Mangles, G. Genoud, S. Kneip, M. Burza, K. Cassou, B. Cros, N. P. Dover, C. Kamperidis, Z. Najmudin, A. Persson, J. Schreiber, F. Wojda, and C. G. Wahlström, "Controlling the spectrum of x-rays generated in a laser-plasma accelerator by tailoring the laser wavefront," *Appl. Phys. Lett.* **95**, 181106 (2009).
44. M. J. Streeter, S. J. Dann, J. D. Scott, C. D. Baird, C. D. Murphy, S. Eardley, R. A. Smith, S. Rozario, J. N. Gruse, S. P. Mangles, Z. Najmudin, S. Tata, M. Krishnamurthy, S. V. Rahul, D. Hazra, P. Pourmoussavi, J. Osterhoff, J. Hah, N. Bourgeois, C. Thornton, C. D. Gregory, C. J. Hooker, O. Chekhlov, S. J. Hawkes, B. Parry, V. A. Marshall, Y. Tang, E. Springate, P. P. Rajeev, A. G. Thomas, and D. R. Symes, "Temporal feedback control of high-intensity laser pulses to optimize ultrafast heating of atomic clusters," *Appl. Phys. Lett.* **112**, 244101 (2018).
45. J. Werschnik and E. Gross, "Quantum optimal control theory," *J. Phys. B: At. Mol. Opt. Phys.* **40**, R175 (2007).